ACS APPLIED MATERIALS & INTERFACES

Research Article

www.acsami.org

Role of Surface Oxides in the Formation of Solid–Electrolyte Interphases at Silicon Electrodes for Lithium-Ion Batteries

Kjell W. Schroder,[†,‡,§] Anthony G. Dylla,[‡,§] Stephen J. Harris,[∥] Lauren J. Webb,[†,‡,§] and Keith J. Stevenson*[,†,‡,§]

[†]Materials Science & Engineering Program, Texas Materials Institute, [‡]Center for Nano- and Molecular Science and Technology, [§]Department of Chemistry, The University of Texas at Austin, Austin, Texas 78712, United States

[∥]Materials Sciences Division, Lawrence Berkeley National Laboratory, Berkeley, California 94720, United States

Supporting Information

ABSTRACT: Nonaqueous solvents in modern battery technologies undergo electroreduction at negative electrodes, leading to the formation of a solid–electrolyte interphase (SEI). The mechanisms and reactions leading to a stable SEI on silicon electrodes in lithium-ion batteries are still poorly understood. This lack of understanding inhibits the rational design of electrolyte additives, active material coatings, and the prediction of Li-ion battery life in general. We prepared SEI with a common nonaqueous solvent ($LiPF_6$ in PC and in EC/DEC 1:1 by wt %) on silicon oxide and etched silicon (001) surfaces in various states of lithiation to understand the role of surface chemistry on the SEI formation mechanism and SEI structure. Anhydrous and anoxic techniques were used to prevent air and moisture contamination of prepared SEI films, allowing for more accurate characterization of SEI chemical stratification and composition by X-ray photoelectron spectroscopy (XPS) and time-of-flight secondary ion mass spectrometry (TOF-SIMS) depth profiling. Additionally, multivariate statistical methods were used to better understand TOF-SIMS depth profiling studies. We conclude that the absence of native-oxide layer on silicon has a significant impact on the formation, composition, structure, and thickness of the SEI.

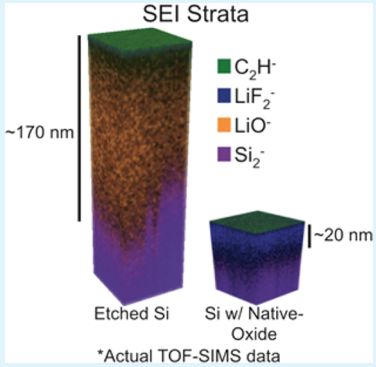

KEYWORDS: *lithium-ion batteries, solid–electrolyte interphase, SEI, TOF-SIMS, XPS, PCA*

1. INTRODUCTION

The solid–electrolyte interphase (SEI) is a chemically complex,[1−6] inhomogeneous[7−9] region found at the surface of electrode materials in nonaqueous electrolytes that are common in lithium-ion batteries (LIBs). Work has been performed over the past 25 years[10] to characterize SEI at graphitic negative electrodes in carbonate electrolytes, as they relate to LIB systems. The SEI plays a central role in the charge-transfer processes,[11] capacity fade,[12] and safety,[13] so its presence and function are of great interest. However, the fundamental mechanisms that control the composition, structure, and performance of the SEI in carbonate-based electrolytes across materials systems other than graphite and on positive electrode materials remain poorly understood. This inhibits significant progress toward rational improvement of LIBs and next-generation technologies like Na-ion, Mg-ion, Li–S, and metal-air batteries.

Studies of model systems (e.g., binder-free electrodes investigated by Nie et al.[14]) have shown that the composition of the SEI has a large influence on the performance of the active material. However, one cannot assume that the SEI structure and composition are roughly the same for all negative electrode materials. To date, there is no systematic understanding of the arrangement and composition of the SEI as a function of materials structure, composition, and electrolyte parameters. The SEI resists easy study and analysis because of the large number of variables present involving electrode materials and electrolytes. Additionally, these solid electrode materials and electrolytes can be synthesized from a number of methods, and their chemistry and compositions are complex. As such, there exists a large set of reactants and reactions that can participate in SEI formation. SEI formation studies are further complicated because they are generally undertaken on composite electrodes comprising active material, conductive additives, and binder. This variability leads to results that are often difficult to interpret or reproduce.[10] Furthermore, the study of SEI structure and composition has been shown by us and others[15−18] to be very sensitive to exposure to ambient conditions because of its reactivity with oxygen and water.

All silicon surfaces are reactive with oxygen and form silicon oxides (SiO_x), the exact composition of which is dependent on the reaction conditions. The role of the silicon oxide in active material performance is still poorly understood, with many conflicting accounts in the literature.[19−23] We are motivated in particular by previous studies of SEI on HOPG graphite by Peled et al.[8] and on Sn surfaces by Kostecki, Lucas and co-

Received: September 23, 2014
Accepted: November 17, 2014
Published: November 17, 2014

workers[24−26] that have isolated surface chemistry effects on SEI composition and structure. To enhance our understanding of SEI composition, structure (stratification/arrangement), and evolution, we investigated SEI formed on a model system of crystalline silicon (001) surfaces with and without a native oxide and in different states of lithiation. We extend the use of our anhydrous and anoxic methods[15] to time-of-flight secondary ion mass spectrometry (TOF-SIMS) depth profiling. The flatness of the wafer enables quantification of the TOF-SIMS depth profiling of SEI as a function of depth, as suggested by Veryovkin et al.[18] We discuss these results in the context of the electrochemistry, XPS spectra, and SEI formation mechanisms to elucidate previous observations of SEI composition (e.g., TOF-SIMS by Xiao et al.[27]). Inspired by Graham et al.,[28] Pacholski et al.,[29] and Muramoto et al.,[30] we employed principal component analysis (PCA) to understand the TOF-SIMS depth profiles. Multivariate analysis (MVA), in general, and PCA, in particular, use statistics to compare entire mass spectra against each other and highlight trends in data that may otherwise be difficult to distinguish if comparing only a small number of secondary ion signals. This approach differs from previous studies of SEI by TOF-SIMS that focused exclusively on utilizing univariate analysis. In this work, MVA, combined with traditional univariate depth profile analysis, isotope-labeling of SEI species, and correlative XPS data, results in a holistic picture of SEI structure and composition. We provide further evidence that the SEI is inhomogeneous in inorganic and organic composition and porous, in agreement with previous reports of Harris, Lu, and co-workers[31−33] and Sheldon and co-workers.[34,35] We discuss structural similarities and differences of SEI formed on etched silicon and native-oxide silicon samples, as well as likely SEI formation mechanisms, highlighting how a powerful toolset of multiple analytic methods coupled with statistics can be used for understanding the formation of inhomogeneous interfacial films of complex structure and chemical composition.

2. EXPERIMENTAL METHODS

Model silicon electrode systems with SEI were prepared on silicon wafer (001) substrates, both with native oxide and oxide-free via reactive ion etching. The electrodes underwent potential sweep and potential step lithiation/delithiation cycles to explore different kinetic and thermodynamic dependences of the formation of the SEI and its resultant structural and compositional components. The resulting systems were analyzed by TOF-SIMS and XPS, closely following methods described previously,[15] ensuring all electrochemistry, spectroscopy, and surface analytical measurements were conducted under anoxic and anhydrous conditions with minimal exposure to oxygen and water.

2.1. Electrochemistry and SEI Formation on Silicon Surfaces. Substrates of single-side polished, nondoped silicon (001) wafers (University Wafer) were cleaned: first, by sequential washing with acetone, isopropyl alcohol, and DI water followed by room-temperature piranha (3:1 concentrated H_2SO_4 (98%) to H_2O_2 (30%)) washing for 1 h and subsequently washed with DI water. To help with electrical contact to the wafer and to control resistance, metal (Cu or Al, Kurt J. Lesker) was evaporated by physical vapor deposition (Cooke Vacuum Products) onto the unpolished side of the silicon wafer.

All silicon wafers had a native-oxide layer (SiO_x), with $2 > x \geq 0.8$, that was measured to be ∼2 nm via spectroscopic ellipsometry (M-2000D spectroscopic ellipsometer, J.A. Woollam). A subset of wafer substrates was etched via reactive ion etching (RIE) (Oxford Instruments Plasma Lab 80+) by a mixture of C_4F_8, O_2, and Ar plasma (the details of these processes are discussed in more detail in the Supporting Information). Etched substrates were then transported within 5 min into an argon-filled glovebox (MBraun) to limit the regrowth of silicon oxides. Subsequent measurement of the surface showed a reduction in the oxide species present on the surface; XPS data of native oxide and etched silicon is included in the Supporting Information (Figure S1).

The cleaned substrates and etched substrates were then configured as the working electrodes in a pseudo-three-electrode electrochemical cell, with lithium metal counter and reference electrodes. A Viton O-ring was used to secure the working electrode in place and to ensure that all electrochemical measurements were undertaken with the same surface area for the working electrode. All electrochemistry was performed with a CH Instruments 660D potentiostat in an argon-filled glovebox (MBraun) containing less than 0.1 ppm water vapor and less than 5.0 ppm oxygen. The electrolyte was composed of 1 M $LiPF_6$ (BASF) dissolved in (1) ethylene carbonate (EC) and diethyl carbonate (DEC), 1:1 by weight (BASF, battery grade); (2) propylene carbonate (PC) (Alfa Aeser); or (3) deuterium-labeled propylene carbonate (CDN Isotopes), molecular formula $C_4D_6O_3$ (dPC).

SEI was formed on electrodes in EC/DEC electrolyte via potential sweep voltammetry and multiple potential-step chronoamperometry. Electrode surfaces and SEI are identified in the Results and Discussion section by the electrochemical method used to prepare them in order to correlate these methods with their surface chemistry properties. All experiments proceeded from open-circuit potential, OCV (which ranged from 3.2 to 2.8 V). Lithiated electrodes with SEI were prepared by stepping the potential from OCV to 0.01 V and holding for 300s (lithiated by chronoamperometry; CA) and by a single potential sweep from OCV to 0.01 V at 10 mV s^{-1} scan rate (linear sweep voltammetry; LSV). Delithiated electrodes were prepared by stepping the potential from OCV to 0.01 V, holding for 300 s, then stepping the potential to OCV and holding for 300 s (delithiated by chronoamperometry, DCA), and by sweeping the potential from OCV to 0.01 V to OCV at 10 mV s^{-1} for a number of cycles (cyclic voltammetry, CV). Time duration, potentials, and scan rates were chosen to enable investigation of the competition between SEI reactions and lithiation/delithiation reactions as well as to facilitate easy comparison to previous data.[15]

For SEI prepared in deuterated-PC and PC electrolytes, native-oxide silicon electrodes underwent sequential potential-step chronoamperometry experiments. The first potential step was from OCV to 0.01 V for 300 s and was followed by washing with PC, and baking on a hot plate at ∼30 °C for 40 min to evaporate any remaining solvent. Finally, the electrode was reconfigured as a working electrode and underwent a second potential step from the original OCV to 0.01 V for 300 s.

Immediately following the electrochemistry, the electrolyte, reference electrode, and counter electrode were removed from the cell, and the silicon electrodes were electrically disconnected and washed three times with 1−3 mL of solvent. For SEI prepared in EC/DEC solvent, 99.999% DEC (Alpha Aeser) in molecular sieves was used to wash the electrode. For SEI prepared in PC or dPC solvent, 99.999% PC (Alpha Aeser) in molecular sieves was used to wash the electrode.

The electrodes were then moved into a time-of-flight secondary ion mass spectrometer (TOF-SIMS) or X-ray photoelectron spectrometer (XPS) using a built in-house reduced oxidation (ROx) interface carefully designed for transferring air-sensitive samples from a glovebox to an ultra-high-vacuum environment. The ROx interface contains pumping controls and a set of built-in figures of merit that are used to verify that samples were not exposed to additional traces of oxygen and water during transfer. The methods used are proprietary and described in further detail elsewhere.[36] After multiple electrodes were adhered to a sample bar by either double-sided carbon or copper tape, the bar was sealed in the ROx interface and then loaded into the UHV instruments.

2.2. X-ray Photoelectron Spectroscopy. Photoelectron spectra were collected using a Kratos Ultra DLD XPS and analyzed along the same methods used in our previous work.[15] All XPS measurements were collected with a 300 × 700 μm^2 spot size, and a charge

neutralizer was used during acquisition of most spectra. Survey scans were collected with a 1.0 eV resolution, followed by high-resolution 0.05 eV 1 s scans of the carbon 1s, oxygen 1s, lithium 1s, silicon 2p, fluorine 1s, and phosphorus 2p regions.

Fits to the XPS spectra were performed with CasaXPS software (version 2.3.15, Casa Software Ltd.) to estimate the atomic compositions and chemical species comprising the SEI. All fitting followed a self-consistent method similar to what we have previously reported, and an example fit is given in the Supporting Information (Figure S2). All SEI species were assumed to be electronically insulating and were therefore fitted with linear backgrounds. All peaks were fit by Voight functions composed of 15% Lorentzian and 85% Guassian; previous work has used Voight functions with 5−30% Lorentzian composition.[10,19,37−40] Initial peak fits were made of the spectra using a Levenberg−Marquardt least-squares algorithm, and functionalities were assigned based on the difference in binding energies between the fitted Voigt functions. Atoms in the same functionality were assumed to be stoichiometric, and the areas of the fitted functions were set equal to each other after correcting for relative sensitivity factor. The resulting spectra were then refit and to compensate for any charging during the measurement, all spectra were shifted relative to the binding energy of the carbon 1s sp^3 oxidation state (assigned to 284.8 eV). The sum of the areas under the peaks were then used to determine relative composition of the outermost ∼10 nm of the SEI.

2.3. Time-of-Flight Secondary Ion Mass Spectrometry. Time-of-flight secondary ion mass spectrometry (TOF-SIMS) data was collected using a TOF.SIMS 5 by ION-TOF GmbH (Germany), with a mass resolution better than 8000 ($m/\Delta m$). Bi_3^{2+} (0.9 pA) accelerated at 30 keV were used as the analysis (primary) gun and Cs^+ (65 nA) accelerated at 1 keV, as the sputtering (secondary) gun. The depth profiling experiments were performed in static mode where the sputtering gun (Cs^+) was operated for 1.0 s over a 300 × 300 μm^2 area of the electrode surface followed by the analysis gun (Bi_3^{2+}) over a sawtooth-rastered 100 × 100 μm^2 area centered in the sputtering crater. This sputter/analysis sequence was cycled until a steady-state signal from Si_2^- in the depth profile was observed, indicating full penetration of the SEI. Secondary ions were detected in negative ion mode, and a full spectrum from 1 to 1000 amu was acquired. All analysis was performed with main analysis chamber pressures between 2 and 9 × 10^{-9} mbar.

TOF-SIMS spectra underwent analysis using proprietary ION-TOF software (version 6.3). To ensure an accurate mass calibration, a set of only inorganic peaks[41] comprising at least six of $^6Li^-$, Li^-, OH^-, LiO^-, Li_2F^-, Si^-, SiO^-, Si_2^-, Si_3^-, Si_4^-, and Si_5^- was carried out so that the largest deviation for any calibrant ion was no greater than ±30 ppm. A set of 329 peaks regularly found across the depth profiles was assembled, and the signal of those peaks as a function of sputtering time was compiled. The depth profile data was then analyzed using a homemade script executed in the iPython nootbook environment utilizing the numpy, scipy, and pandas libraries.[42−45] The script organized the data, normalized and centered each spectra, found the correlation matrix of the secondary ions, and carried out principal component analysis by singular value decomposition.

2.4. Optical Profilometry. After depth profiling, samples were removed from the TOF-SIMS, and sputtering craters were analyzed by optical profilometry (Veeco, NT9100 Optical Profiler). Optical profiles of the TOF-SIMS sputtering craters were matched with their corresponding TOF-SIMS depth profile data. Two-dimensional height profiles were rendered for each crater, and the step height between the bottom of the sputtering crater and the top of the exposed SEI was determined by averaging the vertical (y axis) displacement between two sections of 10−100 μm in the 2D height profiles; an example is given in the Supporting Information (Figure S3). This process was repeated for at least four 2D height profiles of each crater, and the reported depth of the crater for each sample is the median of these measurements.

Sputtering times and crater depths were then used to determine sputtering rates for both the SEI layer and the wafer by a linear fit of the sputtering depth vs sputtering time data. The resulting sputtering rates were used to transform sputtering time into depth using a simple two-layer sputtering model, following Zimmerman et al.[46] and Elko-Hansen et al.[47] The Si_2^- mass fragment signal was used to define the relative contributions of each sputtering rate in the transition between the SEI and the silicon active material. The minimum value of the secondary ion signal of Si_2^- was subtracted from the maximum value of the Si_2^- signal for each depth profile; the sputtering depth where the Si_2^- signal was half of this difference was taken as the outer surface of the silicon active material.

3. RESULTS AND DISCUSSION

3.1. Electrochemistry of Etched and Oxide-Covered (100) Silicon Wafer. In our previous work,[15] Si 2p XPS spectra indicated that after electrodes underwent SEI formation and were exposed to air there was an increase in silicon surface functionalities. We proposed that oxygen reacted with the silicon surface, causing a regrowth of the oxide layer. Regardless of the mechanism, the surface was observed to be reactive, suggesting that the native oxide had been either (1) reduced during lithiation of the electrode or (2) that some product during the electroreduction of the electrolyte had further reacted with the oxide. The lithiation of native-oxide films on silicon electrodes has been previously observed, but there remains a disagreement in the literature about the reversibility of this reaction.[19,48−50]

Cyclic voltammetry (Figure 1) was performed on both native-oxide (Figure 1a) and REI-etched (Figure 1b) silicon electrodes using 1 M $LiPF_6$ in EC/DEC (1:1 by wt %). All potentials are reported vs lithium−metal/lithium-ion redox couple (i.e., V vs Li/Li^+). We have previously discussed the electrochemical lithiation and delithation behavior of silicon wafer electrodes in the context of other silicon systems,[15] and the results reported here are similar. However, there are apparent and repeatable differences between the electrochemistry of the etched silicon and native-oxide silicon electrodes.

First, the current scales in Figure 1a,b differ by an order of magnitude. This observation held true for all experiments; regardless of whether potential sweep voltammetry or potential-step chronoamperometry was employed, the etched silicon produced higher current measurements than that of the same experiment performed on silicon with native oxide. We attribute the difference in current (and consequently, current density) to the increased conductivity of the etched silicon surface compared to that of the native-oxide silicon surface, as both electrodes underwent the same cleaning and electrochemical treatment.

Both of the electrodes of Figure 1 were electrically connected by an aluminum metal back contact (i.e., via a metal-oxide interface). By choosing a different metal to evaporate onto the silicon electrode, it is possible to tune the resistance at this metal-oxide interface (and the resulting Schottky barrier). Higher resistance leads to lower background current, and we have observed that it further diminishes the signal from lithiation in comparison to surface-confined reactions (e.g., background current). Both the etched silicon (Figure 1b) and the native-oxide silicon electrodes (Figure 1a) included an aluminum back contact to exploit this phenomenon and to enable easy observation of surface-confined reactions on the electrode. As a consequence, we are able to discuss electrochemical behavior that we had previously not identified.[15]

Reduction reactions (observed as negative current peaks) due to lithiation were observed at both the etched and native-oxide silicon electrodes, as well as oxidation reactions (observed

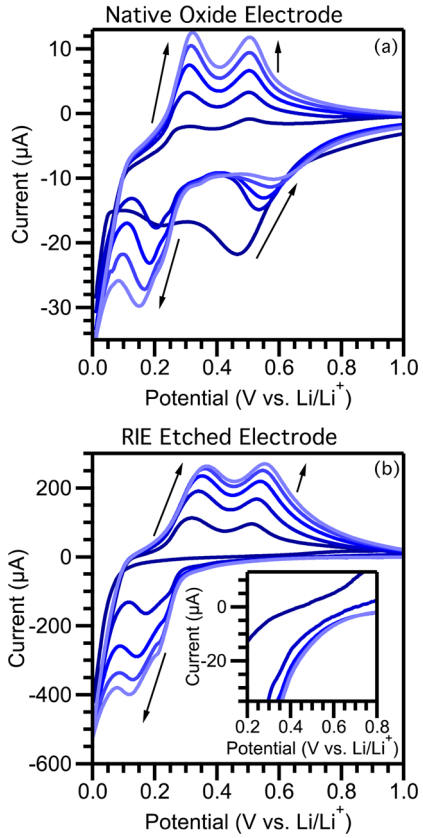

Figure 1. Representative cyclic voltammograms using 1 M $LiPF_6$ in EC/DEC (1:1 by wt %) and (100) silicon wafer working electrodes, (a) with a native oxide and (b) with a RIE etched surface. Both electrodes were cycled from OCV (~3.0 V) to 0.01 V Li/Li^+ at 10 mV s^{-1} scan rate for 5 cycles. Cycles are distinguished by hues, starting with the darkest (navy) and decreasing to the last cycle (light blue). Arrows next to the data indicate the trend in current growth or diminishment with cycling. The difference in current scales between panels a and b should be noted; an inset in panel b with current scaled the same as that in panel a shows the absence of peaks between 0.47 and 0.59 V.

as positive current peaks) due to delithiation. Table 1 summarizes the peak potentials at which etched and native-oxide silicon electrodes underwent the lithiation and delithiation processes shown in Figure 1. Only one clearly defined lithiation peak is observed, and two clearly defined delithation peaks for each cycle are seen for both etched and native-oxide silicon electrodes. The two oxidation peaks are attributed to a phase transformation from low to high lithium concentration in the lithium–silicon alloy at less positive potential and complete delithation at the more positive potential.[51]

Table 1. List of Values for the Peak Potentials (E_p) of the Observed Lithiation, Oxide Reduction, and Delithation Reactions for the Two Representative CVs Shown in Figure 1

	oxide reduction peak potential (V)	lithiation peak potential (V)	1st delithiation peak potential (V)	2nd delithiation peak potential (V)
oxide, 1st cycle	0.226	0.465	0.310	0.502
2nd cycle	0.205	0.534	0.307	0.503
3rd cycle	0.183	0.551	0.310	0.503
4th cycle	0.167	0.573	0.316	0.503
5th cycle	0.150	0.588	0.320	0.504
etched, 1st cycle	n/a	n/a	0.319	0.513
2nd cycle	0.169	n/a	0.335	0.521
3rd cycle	0.238	n/a	0.352	0.531
4th cycle	0.134	n/a	0.361	0.547
5th cycle	0.118	n/a	0.368	0.547

While the differences between the etched and native-oxide silicon electrodes were clear, a few features of the lithiation behavior remained the same. For example, lithiation was suppressed in the first cycle of both etched and native-oxide silicon electrodes. Previously, we suggested that this behavior was due to the reduction of the native-oxide layer;[15] however, the suppression of current is present in the first cycle of the CV of the etched electrode (Figure 1b) as well as in the CV of the native-oxide silicon electrode (Figure 1a). Given this observation and our identification of the reduction reaction peak (discussed below) for native oxide on silicon, we attribute the behavior to mechanical resistance by the silicon to accommodating lithium ions for the first time (e.g., compressive strain and surface tension). After each successive cycle, the electrodes were conditioned to some extent (through a diffusion-induced solid-state amorphization mechanism), and lithiation and delithiation currents increased.

CVs of both the etched and native-oxide silicon electrodes showed that lithiation reaction potentials shift to less-positive values with increasing cycle and that delithiation potentials shift to more-positive values with increasing cycle (Figure 1 and Table 1). Again, we have previously addressed this behavior to a degree,[15] and we emphasize the role of continued amorphization and the dynamic nature of the silicon electrode surface. The proposed mechanism to explain this observation is that the amorphization of the silicon that occurs upon lithation[52−55] leads to an increased quantity of active material during succeeding lithiation. However, the amorphous silicon is less conductive than that of the crystalline form, and this may be the reason for the increasing overpotential. Additionally, continued SEI evolution and the charge transfer resistance[56−58] may be playing a role in the increased overpotential of the lithiation and delithiation reactions in silicon.

From careful inspection of both CVs, there was also an apparent increase in current in cycles 2−5 at potentials slightly more positive than the above-mentioned reduction peaks, although there is no local maximum (true electrochemical peak). A shoulder at ~0.225 V in each cycle of the oxide electrode CV (Figure 1a) and at ~0.220 V in the etched electrode CV (Figure 1b) was observed. We attribute these shoulders (or prewaves) to a second lithiation reaction, matching the two-step oxidation behavior discussed above. We also observe an increasing overpotential for the prewave with each cycle (a shift to less-positive potential with each cycle) in both the etched and native-oxide silicon electrodes. We leave more precise measurement of this overpotential shift to further investigation; it requires peak fitting, a novel electrochemical background correction technique, and/or multiphysics modeling to be quantified.

The most significant difference between the electrochemistry of the etched and native-oxide electrodes is the presence of a reduction peak in Figure 1a that is not present in Figure 1b. This reduction peak has an E_p between 0.47 and 0.59 V (Figure 1a and Table 1). Because of our previous observations about

the reactivity of the silicon surface after exposure to air[15] and the fact that the peak is present only in the CV of the oxide electrode, we attribute it to the at least partial reduction of the native-oxide layer (Reaction 1).

$$SiO_y + XLi^+ + Xe^- \rightarrow Li_xSiO_y \quad (1)$$

Silicon oxide has previously been observed to undergo partial reduction by Philippe et al.[19] and Radvanyi and co-workers.[48−50] The inset of Figure 1b (RIE-etched electrode) shows the reductive current of cycles 1−5 in a potential range where the peak for Reaction 1 would be expected to be scaled to the current of Figure 1a; no peak was observed.

3.2. SEI Composition on Etched and Oxide-Covered Electrodes from XPS Fitting. In addition to differences in electrochemistry, there are also differences in SEI structure and composition when comparing the etched and native-oxide silicon electrodes. Figure 2 shows a bar graph indicating the relative compositions of the SEI on both etched and native-oxide silicon electrodes formed from two different electrochemical techniques, as derived from fitting of XPS spectra (shown in the Supporting Information, Figure S2). For each of the etched and native-oxide silicon electrodes investigated by XPS, one set underwent cyclic voltammetry (CV) and a second set underwent a potential step chronoamperometry (CA). All electrochemistry was done with 1 M $LiPF_6$ in EC/DEC (1:1 by wt %) electrolyte.

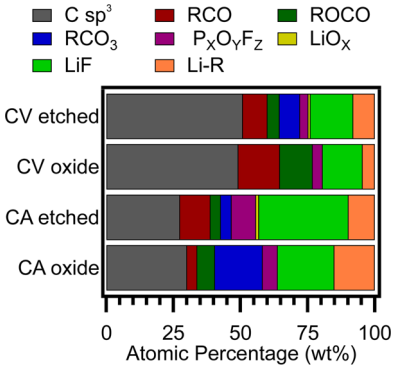

Figure 2. Relative composition of the outermost ∼10 nm of SEI formed on etched and native-oxide silicon electrodes via CV and CA. New fits are included of the native-oxide silicon electrodes from XPS spectra that was previously published.[15]

The resulting spectral fits provide the relative composition (in terms of functionalities) of an outer volume of the SEI. Because the inelastic mean-free path of photoexcited electrons limits the XPS probing depth to ∼10 nm, the compositions shown in Figure 2 are only representative of the outermost portion of the SEI, farthest from the SEI/silicon interface (i.e., the ∼10 nm of SEI closest to the solvent when the silicon electrode was configured in the cell). In previous work, we limited our observations to SEI formed on native-oxide silicon electrodes and found that the thickness of the SEI was on the order of the XPS probing depth, implying that these results gave a good overview of the entire SEI chemistry. However, that is not the case for all of the SEI films investigated in the present study, as is discussed below in the context of the TOF-SIMS depth profiling experiments.

On the basis of the compositions shown in Figure 2, there are subtle differences in the chemistry of the SEI across different electrode surfaces and electrochemical treatments. In all of the electrodes investigated, organics made up at least a plurality (if not a majority) of the functionalities observed within the outer ∼10 nm of SEI. Species labeled C sp^3 in Figure 2 are aliphatic carbon in general and may include adventitious carbon. Oxygen containing species are labeled RCO for alkoxy groups (ethers and alkoxides) and ROCO for carboxyl groups (carboxylates, esters), but may also contain oxalates. Carbonates are labeled RCO_3 and include carbonic esters and ionic carbonate salts. These species have been previously reported to be part of polymers and oligomers, including polyolefins,[9] poly(ethylene oxide) (POE)-like, and poly(ethylene glycol) (PEG)-like species. We find that SEI formed by CA contained 45−60% organic functionalities and SEI formed by CV contained 70−80% organic functionalities. Additionally, more organic species are formed on the oxide-covered electrodes than that on the etched electrodes.

Inorganic functionalities like lithium fluoride (Figure 2, LiF) and fluoro- and phosphoro-oxides ($P_xO_yF_z$) were more prevalent on the etched silicon electrodes than on native-oxide silicon electrodes and on electrodes that underwent CA over those that underwent CV. Both of the etched silicon electrodes show a small, but nontrivial, amount of lithium oxide (LiO_x). It can be difficult to distinguish among hydroxide, peroxide, and oxide compounds by XPS, so this assignment may also include these functionalities as well. The balance of the SEI of each silicon electrode included ionic lithium ions (Li-X) bound to either the fluoro- and phosphoro-oxides or organics such as lithium alkoxide, lithium carboxylate, lithium carbonate salt, and carbonic esters (which cannot be distinguished by XPS). Additionally, lithium included in the Li-X functionalities, as well as oxygen attributed to $P_xO_yF_z$, may, in fact, be part of lithium−silicon oxide (Li_xSiO_y) following Philippe et al.[19] and Radvanyi and co-workers;[48−50] however, we observed no appreciable Si 2p peaks with binding energy in the regions previously reported, and little Si 2p signal in general. We note that LiO_x (e.g., Li_2O) was not found to any significant degree on the oxide electrodes.

We propose that the variations in the SEI composition are explained by the kinetics of the competing SEI formation reactions and the electronic and chemical differences between the etched and native-oxide silicon electrodes. Before we present these mechanisms in detail, further observations of the chemistry and structure of the SEI will be presented in the context of the TOF-SIMS depth profiles, below.

3.3. Depth Profiles of SEI Formed on Etched and Oxide-Covered Electrode. TOF-SIMS depth profiling was used to explore further the differences in structure between SEI prepared on oxide-covered and etched electrode surfaces. Extensive work has been done on understanding the depth profiling of organic films on hard surfaces (typically silicon). For example, work by Cheng et al.,[59,60] Brison et al.,[61] Cramer et al.,[62] Seah et al.,[63] and Gillen and Roberson[64] has shown that the choice of analysis and sputtering beam species (as well as beam energies) can exacerbate matrix effects at the surface of a sample, amplify back-reflection effects due to projectile-deposited energy at hard substrate/organic interfaces, cause sample damage, mixing of layers, and change in secondary ion signal. As a consequence, we chose Cs^+ as a low-energy sputtering source and polyatomic Bi_3^{2+} as the analysis source to increase ion yields and minimize sample damage.[61−63] Also, we take careful note of features in the depth profiles that could be attributed to matrix effects or back-reflection effects. Studies of organic films are often done by detecting positive secondary

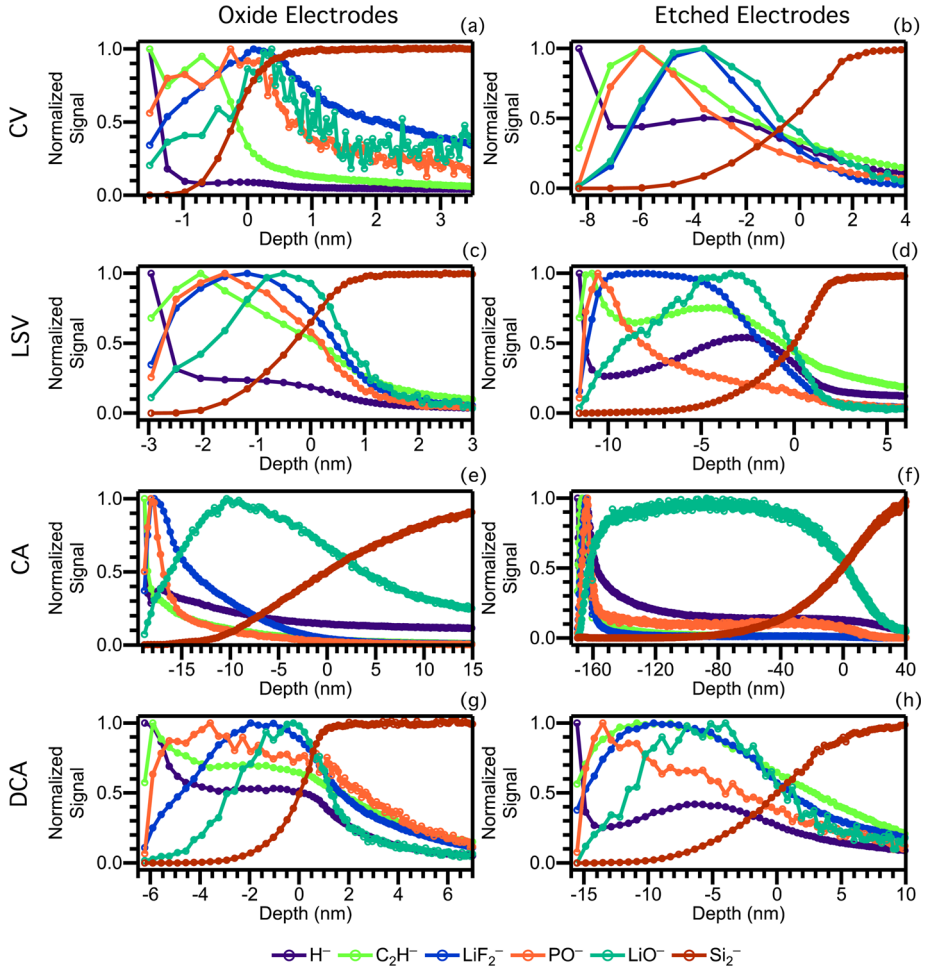

Figure 3. TOF-SIMS depth profiles of both native-oxide (left column) and etched (right column) silicon electrodes that have undergone (a, b) 4 cycles of cyclic voltammetry from OCV to 0.01 V at 10 mV s^{-1} (CV), (c, d) linear sweep voltammetry from OCV to 0.01 V at 10 mV s^{-1} (LSV), (e, f) potential step chronoamperometry from OCV to 0.01 V for 300 s, (g, h) two 300 s potential steps, one from OCV to 0.01 V followed by a second from 0.01 V to OCV. It should be noted that each subfigure is plotted on its own *x*-axis scale; the thickness of each SEI varies significantly among the electrochemical methods' electrode surfaces. The depth profiles were plotted on their own scales to better see the changes in each secondary ions' normalized signal. Negative depths are above the surface of the silicon electrode, and positive depths go below the surface, into the wafer.

ions;[65,66] however, positive ion mode is more amenable to the use of O^- sputtering ion than Cs^+ sputtering ions. Because of the highly sensitive nature of the SEI to exposure to oxygen,[15−18] Cs^+ sputtering ions (and thus negative ion mode) were chosen instead of O^- sputtering ions.

The depth profiles themselves are not trivial to interpret. Cheng et al.[59] proposed a simple erosion model for molecular SIMS depth profiling. The model was developed for a single combined primary and sputtering ion beam instrument and found good agreement with experiment. That being said, many of the assumptions made by the Cheng et al. model also hold for our dual-beam experiments; in particular, they assume that profiles of signals of secondary ion signals resulting from molecular films are proportional to ion yield. Cheng et al. further suggest that this is a sufficient condition to conclude that concentration is proportional to signal because the ion yields of daughter fragments are proportional to the concentration of parent species that fragmented.

For the depth profiles in Figure 3, we present our results as qualitative indications of the chemistry. All of the work cited above took place in simplified model systems with well-defined order, density, and controlled chemical composition, none of which is true of the SEI we investigated. Piwowar et al.[67] showed that, in model biological systems, mixing salts with organic species can suppress the signal detected from the organic species. Additionally, work by Gnaser[68] has shown that implantation of Cs^+ ions during sputtering can change the work function of the surface under investigation and, in turn, effect secondary ion signal. For all of the above reasons, we do not compare relative concentrations between different species on the basis of secondary ion signal. Instead, with respect to Figure 3, we have (1) used the XPS results above as a guide for choosing marker species to represent different components of the SEI, (2) normalized each marker species to its maximum signal in the depth profiles in Figure 3, (3) assumed that the ion signal is proportional to the yield of the daughter fragment, which is, in turn, proportional to concentration of the parent molecules, and (4) restricted our interpretation to comparing secondary ion concentrations across a depth profile and not between different secondary ions.

The results from depth profiles for eight representative experiments are shown in Figure 3. As discussed with respect to the experimental methods, the Si_2^- mass fragment signal measured in each mass spectrum was used to identify the interface of the SEI with the silicon active material in each depth profile and to calibrate a linear combination sputtering

model that results in a quantitative depth analysis of the SEI strata. Depth resolutions (i.e., the slope of the Si_2^- signal) of the electrodes vary because of SIMS instrumental parameters as well as general SEI heterogeneity, surface-roughness, RIE-induced surface damage, and electrochemically induced surface damage. Additionally, there is an apparent overlap between SEI ion species into the silicon strata that is an artifact of all of the conditions discussed with respect to depth resolution and also due to knock-in of SEI species into the silicon surface. Depth is plotted relative to 50% of the maximum Si_2^- signal, which was defined as the origin (depth of 0 nm), with positive depths defined as being into the surface of the silicon and negative defined as being above the SEI/silicon interface.

Figure 3 shows clearly that the thickness of the SEI varies greatly across the different preparation methods and the two electrode surface chemistries. A summary of the estimated thickness of each SEI depth profile shown in Figure 3 is listed in Table 2. In general, the SEI prepared on etched silicon electrodes were thicker than the SEI prepared by the same electrochemical method on the native-oxide silicon electrodes. Additionally, the SEI on lithiated silicon electrodes (CA, LSV) were thicker than the SEI on delithiated silicon electrodes (CV, DCA).

Table 2. Summary of the SEI Thicknesses for Each Electrochemical Method on Native-Oxide and Etched Silicon Electrodes Shown in Figure 3

	CV	LSV	CA	DCA
oxide SEI thickness (nm)	1.5	3.0	18.8	6.2
etched SEI thickness (nm)	8.3	11.6	169.9	15.5

The chemical structure of the SEI also varied greatly across the different electrochemical methods and electrode surfaces. Previous work, both experimental and computational, has proposed and supported a set of SEI formation reactions.[3−6,69−73] Identifying these formation mechanisms is not the focus of this work, but we would like to briefly discuss specific reactions and reference the XPS results to give context to the depth profiles of Figure 3.

The organic components of the SEI are generally known to result from electroreduction of the solvent and are most likely assisted by lithium ions due to their presence at the surface in the electric double layer. For example, EC undergoes electroreduction to form lithium semicarbonate (Scheme 1), or DEC undergoes electroreduction to form alkoxy and carboxyl functionalities (Scheme 2). These reactions are known to be kinetically limited, rather than thermodynamically limited.[74−76]

Taking the C_2H^- secondary ion as a marker for organic functionalities (such as the aliphatic, alkoxy, carboxyl, oxalate, and carbonate species discussed above in the XPS results of Figure 2), we observe that for all depth profiles, oligomer and polymer species are most concentrated at the outer portion of the SEI (i.e., farthest from the electrode/SEI interface). This accounts for their prominence in the XPS measurements and is entirely consistent with the classic understanding of SEI structure on graphitic electrodes presented Peled and Golodnitsky.[76] Peled and Golodnitsky explain the structure in terms of the forward rate constant (k_e) for the reaction to further reduce the SEI components (Reaction 2):

$$\text{substrate}_{(\text{SEI})} + e^- \rightarrow \text{product} \quad (2)$$

Organic products have a relatively high value of k_e (and thus low kinetic stability) in comparison to that of the other SEI components (e.g., LiF, Li_2O, inorganic species in general). This results in a kinetic selection pressure that eliminates oligomeric and polymeric species from the portion of the SEI nearest the electrode surface.

The kinetic stability theory predicts that organic species may be detectable near the SEI/silicon interface during initial formation of the SEI, but that these species would undergo further reduction as the SEI evolved with continued lithiation. Although not an exact comparison, the C_2H^- ion signal in the SEI formed on native-oxide silicon by LSV (Figure 3c) has more signal from organic species near the SEI/silicon interface than does the SEI formed by CA (Figure 3e). A similar comparison can be made for the SEI formed on etched silicon electrodes under LSV (Figure 3d) and under CA (Figure 3f).

The formation of the inorganic products, such as LiF (Reaction 3), is due to electroless, thermally driven reactions.[77−79]

$$Li^+_{(\text{sol})} + PF^-_{6(\text{sol})} \rightarrow PF_{5(\text{sol})} + LiF_{(\text{s})} \quad (3)$$

These species are observed from the surface of the SEI all the way to the SEI/silicon interface. Again, the higher kinetic stability of these species relative to the organic species implies they should have highest concentration closer to the SEI/silicon interface compared to that of the organic species.

Turning again to the depth profiles in Figure 3, we find Li_2F^- signal overlapping with the organic species, but the highest concentration is generally closer to the SEI/silicon interface. PO^- concentration overlaps with Li_2F^- and is present at higher concentrations closer to SEI/silicon interface in oxide SEI than etched SEI. We take Li_2F^- to be a marker for LiF concentration and PO^- to be a marker for PO_x and $P_xO_yF_z$ species, and we note that the maximum concentrations for the C_2H^-, PO^-, and Li_2F^- all occurred in the outermost 10 nm of the SEI prepared by CV (Figure 3a,b) and CA (Figure 3e,f), in agreement with the XPS results of Figure 2. The LiO^- signal will be discussed in more detail below, but it should be noted that maximum LiO^- concentration is located adjacent to the SEI/silicon interface in all of the depth profiles. In terms of the arrangement of the SEI species, we find that the kinetic stability model accurately predicts the strata of the SEI on the silicon surfaces.

In general, LiO^- fragments may represent species attributed to LiO_x, $P_xO_yF_z$, and Li-X in the XPS results above (Figure 2). The relatively low concentration of corresponding LiO_x species observed in the XPS spectra (Figure 2) is explained by the fact that most of the LiO^- lies below the first ∼10 nm of the SEI.

Scheme 1. Electroreduction of Ethylene Carbonate To Form Lithium Semi-Carbonate

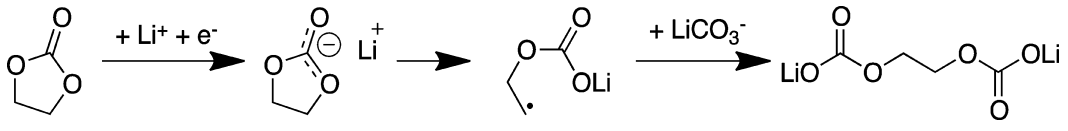

Scheme 2. Electroreduction of Diethyl Carbonate To Form Lithium Ethoxy and a Radical Ethyl Carboxylate

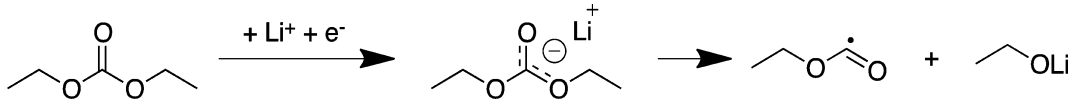

From the XPS spectra, it seems likely that LiO^- originates from Li_2O and/or LiOH species. We suggest that LiOH may also be a parent of the LiO^- ion fragment because, as noted above, the XPS results cannot resolve the difference between OH and O functionalities and the overlap of LiO^- and H^- signals. In general, H^- signal tracks with the signal of the C_2H^- secondary ion, suggesting that H^- mostly originates from hydrocarbons. However, H^- also shows pronounced matrix effects, reflected in the high signal near the outer edge of each SEI and back-reflection near the SEI/Si interface. Additionally, there are regions of H^- signal that overlap with suppressed C_2H^- signal, e.g., −14 to −11 nm in the SEI formed by CA on the oxide surface (Figure 3e) and around −140 nm in the SEI formed by CA on etched surface (Figure 3f).

Li_xSiO_y is another possible parent species of LiO^- for the native-oxide silicon electrodes because, as noted above, it is not ruled out by the XPS results (Figure 2). Organic functionalities (LiOR) are yet another possible source of LiO^-; however, there is good overlap only between the LiO^- and C_2H^- signals in the SEI prepared by LSV (Figure 3c,d) and DCA (Figures 3g and 3h) and CV on an etched silicon electrode (Figure 3b).

The concentration of LiO^- shows the biggest change between etched and native-oxide silicon electrodes. If a region of SEI with high LiO^- concentration is defined as having signal ≥90% of the maximum, then the native-oxide silicon electrodes all show narrower bands of high concentration than those of etched silicon electrodes that underwent the same electrochemical experiments. For example, if we compare the SEI prepared by LSV, then the native-oxide silicon electrode has a region of high LiO^- concentration ∼1.5 nm thick (Figure 3c), and the etched silicon electrode has one ∼5 nm thick (Figure 3d). This difference is especially dramatic when comparing the SEI prepared by CA; the etched silicon electrode (Figure 3f) has a region of high concentration ∼13× thicker than that of the native-oxide silicon electrode (Figure 3e).

The thickness of the LiO^- SEI stratum also varies between lithiated and delithiated electrodes, regardless of the electrode surface. The lithiated silicon electrodes (i.e., SEI prepared by CA and LSV, Figure 3c–f) have thicker regions of high LiO^- concentration than that of the delithiated silcon electrodes (i.e., SEI prepared by CV and DCA, Figure 3a,b,g,h). This data suggests that the majority of the parent species that give rise to the LiO^- signal are formed during lithiation and then reversibly dissolved during delithiation. The reversibility of the reaction further reinforces the claim that the LiO^- originates from Li_2O, and LiOH species. The XPS results and the presence of the LiO^- signal in the etched silicon electrode depth profiles means that these species are not formed from oxygen present in the native oxide. Instead, the oxygen must originate from contaminates such as O_2 or water dissolved in the electrolyte or from the carbonate solvent molecules. While it is possible that the LiO_x species resulted from contaminates, it seems improbable that surface effects and electrochemical effects would have such a repeatable and systematic influence with only trace amounts of O_2 (≤5.0 pmm) and H_2O (≤0.1 ppm) present during electrochemical preparation. Instead, we propose that the oxygen primarily results from reduction of organic carbonate species, with one example being from an alkoxy group (Reaction 4):

$$RCO + 2Li^+ + 2e^- \rightarrow RC^\bullet + Li_2O \quad (4)$$

We have focused most of our discussion of the results around understanding the arrangement of the SEI species as a function of depth, especially in the context of the kinetic stability of the SEI species. However, we have limited ourselves to looking at the spatial concentration of individual secondary ions or comparison among the set of six ions given above. The SIMS experiment, however, results in hundreds of mass peaks for each mass spectrum taken and anywhere from 50 to 500 mass spectra taken in each depth profile. Therefore, a large amount of information has remained unused in our analysis with respect to Figure 3, but the task of identifying the exact parent species in the SEI that gave rise to the daughter fragments that we observe (perhaps through g-SIMS or carefully controlled model SEI), as Veryovkin et al.[18] have proposed to do, is clearly daunting. To ensure the validity of our interpretation, we proceed by other methods to confirm or disconfirm our deductions about the SEI in the next section.

3.4. PCA Analysis of ToF-SIMS Depth Profiles. The analysis of the secondary ions above falls under the term univariate analysis because we have considered individual fragments' concentration as a function of depth. Multivariate analysis (MVA) is a strategy for considering the signal from a set of secondary ions shared by multiple spectra. The goal of MVA, as applied to TOF-SIMS depth profiling, is to look for redundancy in the data set of ion intensities as a function of depth and to exploit any redundancy to facilitate interpretation of the data. For example, two or more secondary daughter ions may result from the same parent species; when interpreting the data, one of those daughter fragments may stand in for all of them. By comparing ion intensities, MVA uses these sets of related secondary ions to compare the chemical composition of the SEI.

Principal component analysis (PCA) is one popular method used to carry out MVA of SIMS data. MVA and PCA are well-known and widely employed methods for analyzing SIMS data from raw spectra,[28,30] to 2D SIMS images,[80−82] to TOF-SIMS depth profiling.[29]

PCA is a statistical approach to dimensional reduction of large sets of variables, used to elucidate trends in data and to enable easy comparisons between results. PCA is often used on data sets with variables that depend on multiple, often colinear and correlated, variables. For the purposes of this study, PCA applied to SIMS spectra effectively produces a new set of compound mass fragments (principal components) that depend on a linear combination of all of the set of considered secondary ions. In terms of the chemistry, PCA compares the relative intensities of every pair of secondary mass fragments to find how highly each pair correlates across the entire data set. For the present analysis, the data set comprises each ion signal, measured at each spectra (depth), of each depth profile. Highly correlated mass fragments are either (1) daughter fragments of the same parent species or (2) daughter fragments of two species that are highly colocalized (share the same ion signal as

a function of depth) across depth profiles. Highly correlated mass fragments are then combined to form the principle components. The PCA analysis produces loadings, which describe how the original mass fragments combine to form the principal components, and scores, which give a value to each spectrum, at a given depth of each depth profile. In this way, the scores give a semiquantitative comparison of the chemical compositions of the compared spectra. As a result, a distance between spectra can be given by plotting the value of the first n principal components for the spectra; spectra that are close together are similar in chemical makeup, and those that are farthest apart are, in turn, most different.

Figure 4 shows the results of the PCA analysis of the depth profiles shown above in Figure 3. Also included in the PCA analysis were depth profiles taken at different locations on those electrodes and depth profiles of additional electrodes prepared in the same manner as those shown in Figure 3. Figure 4a shows the loadings of the organic species, inorganic species (not including those that containing silicon), and silicon-containing species, all of which contribute to both of the first two principal components. Additionally, of the 329 total number of secondary ions used in the PCA, 123 remained unidentified because of multiple possible assignments or no clear assignment. However, a powerful element of PCA analysis is that even these unassigned peaks can contribute to the analysis or the loadings themselves may suggest assignments that would otherwise be missed.[29] The 20 secondary ion fragments with the most impact on the analysis were determined by comparing the distance to the origin (i.e., magnitude) of each secondary ion; these 20 species are listed in order of impact in the Supporting Information (Table S1).

The first set of PCA scores (Figure 4b) includes the depth profiles of the SEI prepared by CA and DCA on native-oxide and etched silicon electrodes (shown in Figure 3e–h). Similarly, the second set of PCA scores (Figure 4c) includes the depth profiles of the SEI prepared by CV and LSV (shown in Figure 3a–d). Each spectrum was assigned a color value based on its depth to allow for qualitative comparison of the chemistry across the SEI and into the silicon electrodes. Plotting the full data set used in the PCA lead to a complicated depiction of the data that inhibited clear interpretation, so we have plotted only the scores of the depth profiles discussed above in Figure 3. However, the full analysis returns common sense results: spectra taken at the same depth, and from SEI prepared by the same electrochemical methods, have scores for PC 1 and PC 2 that are roughly equivalent.

We can observe in Figure 4b,c that spectra from the same depth profile taken at adjacent depths share similar values of PC 1 and PC 2. Additionally, spectra taken from the outermost parts of the SEI depend similarly on PC 1 and PC 2 in general, (PC 1 = -6×10^6 and PC 2 = -2×10^6, approximately), regardless of electrochemistry and electrode surface. The PCA analysis, therefore, confirms our observations about the similar organic makeup of the outermost SEI chemistry shown in the XPS results (Figure 2) and as well the structure discussed above with respect to the univariate analysis (depth profiles of Figure 3).

Figure 4b shows the scores for spectra taken of the profiles of SEI prepared by CA and DCA on both native-oxide and etched silicon electrodes. For the SEI prepared by CA, spectra from the outer organic portions have similar scores, indicating they are chemically similar despite their different silicon electrode surfaces. Scores for spectra taken in the middle of the depth

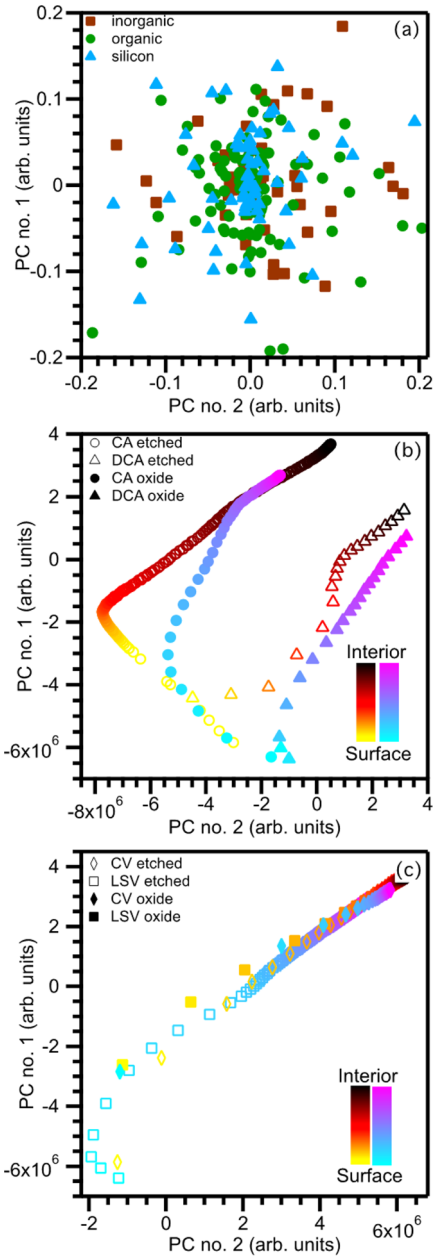

Figure 4. Graphical representation of the principal component analysis of SEI TOF-SIMS depth profiles. The loadings of the mass fragments (a) have been plotted to show that organic (green circles), inorganic (not including silicon, red squares), and silicon-containing (blue triangles) species all contribute to both the first and second principal components. The scores of the eight depth profiles shown above in Figure 3 are plotted with respect to the first and second principal components (b, c). The first two principal components accounted for 31.5 and 15.9% of the variance in the data set, respectively. The scores include spectra from depth profiles of native-oxide silicon electrodes (filled glyphs) and etched silicon electrodes (hallow glyphs) that underwent LSV (squares), CV (diamonds), CA (circles), and DCA (triangles). The hue of the score varies with depth of its associated mass spectra (yellow to dark brown or sky blue to magenta).

profiles of both SEI prepared by CA show a difference in value for PC 2. Considering the XPS results and the concentration of the LiO^- secondary ion in the depth profiles of Figure 3, we attribute this difference to a greater concentration and abundance of LiO_x functionalities derived from Li_2O and LiOH in the SEI prepared by CA on the etched surface. For

spectra deeper in the depth profiles of both native-oxide and etched silicon electrodes that underwent CA, similar scores suggest that both SEI/silicon electrode interfaces are chemically similar, with our explanation being that these spectra all contain primarily lithiated silicon and silicon.

Examining the electrodes that underwent DCA, the outermost SEI show dissimilarity. Looking at Figure 3g,h, the etched silicon electrode has more overlap in concentration among the C_2H^-, PO^-, and Li_2F^- secondary ions, whereas the native-oxide silicon electrode has more layering of strata from organic to inorganic secondary ions. This data explains why the PCA groups the outermost SEI formed by DCA on the etched electrode with SEI compositions found closer to the SEI/silicon interface in the two electrodes that underwent CA. The native-oxide delithiated silicon (DCA) electrode has values of PC 1 and PC 2 of greater similarity to the outer SEI of all of the other electrodes. Spectra from depths closer to the SEI/silicon interface of both electrodes prepared by DCA show greater similarity, until the two deviate again, mostly with respect to PC 2, before spectra from deeper in the electrodes again converge. Again, we take this to be due to differences in SiO_x and LiO_x functionalities: here, at the SEI/silicon interface before both profiles show high concentration of silicon-containing secondary ions.

Figure 4c shows the PCA scores of spectra taken from both native-oxide and etched silicon electrodes that underwent CV and LSV. For the outer, mostly organic, SEI spectra, the PCA scores were more affected by being on an etched vs native-oxide silicon surface than those that underwent the CA and DCA potential step experiments (e.g., the similar scores for the outermost SEI of the electrodes that underwent CV and LSV on native-oxide silicon electrodes). Spectra from the middle of the SEI and approaching the SEI/silicon interface for the etched silicon electrodes show similarity to the outermost SEI spectra of the native-oxide silicon electrodes. Spectra from the SEI/silicon interface and deeper into the electrodes all share similar scores. The fact that all of the inner portions of the electrodes that underwent CV and LSV, as well as those that underwent DCA, share similar scores suggests that all of these spectra have little lithium and are mostly dominated by silicon-containing secondary ions.

In general, the trends presented by the PCA are consistent with our univariate analysis of the depth profiles presented with respect to Figure 3 and the XPS results of Figure 2. We are currently undertaking further development of MVA using other statistical methods (e.g., linear discriminant analysis, partial least-squares regressions, and explanatory factor analysis) on SEI and battery electrode interfaces, especially as explanatory and predictive models for studying electrolyte additives and electrode coatings. Having established that PCA is a useful tool for comparing complex electrochemical interfaces, we hope that these results will serve as an example to extend their use to other complex electrochemical interfaces, as, for example, the inclusion of ionic liquids and impurities in electrodeposited films.[83]

3.5. Deuterium-Labeled Solvent SEI and ToF-SIMS Depth Profiling. As was mentioned briefly in the Introduction, it has been proposed that stable cycling of active materials, like silicon, is dependent on the SEI passivating an electrode's surface and preventing continuous solvent electroreduction (e.g., during initial cycling of an electrode).[84−86] However, the mechanism that was believed to cause this passivation has always been poorly understood. Previous literature on carbonaceous anodes suggest that during the initial lithiation process SEI forms on the negative electrode surface as an insulating layer that blocks further electron transport to the solvent while allowing Li^+ ions to transport to the electrode.[84−86] The resulting insulating layer hypothesis has been used to explain the SEI thickness and the stability of SEI derived from particular solvent and salt combinations in electrolytes.[17,87,88]

These assumptions have also been used to build a mechanical degradation model of SEI evolution on the assumption that mechanical breakup of the SEI allowed for continued growth because the SEI would otherwise be passivating.[22,89] However, recent evidence suggests that this model is not correct and that, instead, solvent transports through a porous SEI.[31−34]

To further investigate the outer, organic-containing SEI structure, TOF-SIMS depth profiles were taken of a set of SEI formed by two sequential potential-step chronoamperometry experiments: one with deuterated propylene (dPC) and one with hydrogen-containing propylene carbonate (PC). In Figures 5 and 6, the TOF-SIMS spectra and depth profiles

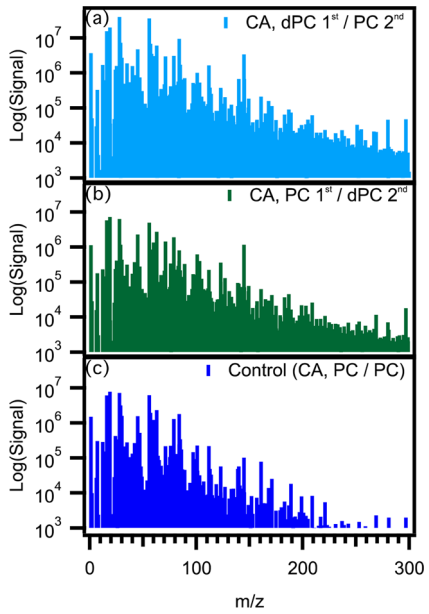

Figure 5. Log plot of the sum of all counts from TOF-SIMS depth profiles for mass fragments with 100 u < m/z < 300 u for SEI formed by two sequential potential step experiments. The salt used was 1 M $LiPF_6$, but the solvent was changed in each potential step: (a) dPC first then PC, (b) PC first then dPC, and (c) a control (PC in both potential steps).

labeled by which solvent was used first and which was used second (e.g., in Figure 5a, dPC was first and PC was second) as well as a control where PC was used in both the first and second potential-step experiments. The purpose of these experiments was to investigate the temporal nature of how the organic species in the SEI were formed (i.e., if the SEI continues to build on top of itself until it reaches a critical thickness) and if the SEI is a porous structure. If the insulating layer model is correct, then deuterated species should be observed in a well-defined layer, either close to the electrode surface if dPC was used first or far from the surface if PC was used first. Deuterium would be observed over the entire SEI, or at least the organic-containing layer of the SEI if it were porous.

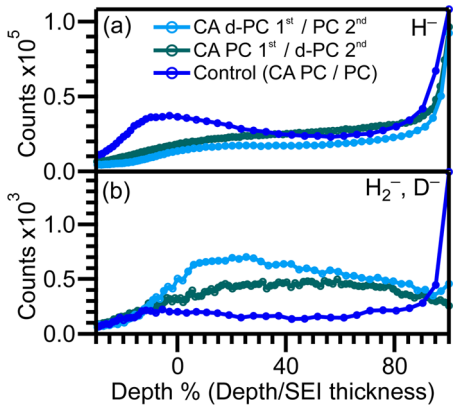

Figure 6. Depth profiles of the SEI for (a) the H^- mass fragment and (b) the convolution of the D^- and H_2^- mass fragments. The *x* axis was rescaled by the thickness of each SEI (i.e., dividing by the maximum *x*-axis value for each profile).

Figure 5 shows the sum of the secondary ion signals across each depth profile for mass fragments with mass-to-charge ratio (m/z) between 100 and 300 u with relative intensities on a log scale. As can clearly be observed, panels a and b in Figure 5 (the SEI formed from dPC electrolytes) show more signal of secondary ions with high m/z than is observed in Figure 5c (the spectra for the control). As we saw in the XPS results and TOF-SIMS depth profiles shown in Figure 3, the SEI formed by CA on oxide surfaces are primarily made up of organic species. The same electrochemical parameters and SIMS analysis and sputtering parameters were used in the preparation and analysis of all of the SEI, so the differences in mass spectra must be a result of the electrolyte used. For this reason, we attribute the heavier organic mass fragments present in SEI species of Figure 5a,b to hydrocarbons containing deuterium, which are species that are absent in the control experiment.

Turning to the TOF-SIMS depth profiles shown in Figure 6, the signal of hydrogen (Figure 6a) and the secondary ion with $m/z \sim 2$ u (Figure 6b) are plotted as a function of the depth. The depth axes were rescaled to the dimensionless parameter depth percentage by dividing the depth in nanometers by the SEI thickness in nanometers in order to account for the variability in SEI thickness in each depth profile and to facilitate the comparison of structure between SEI.

There are two ways to interpret the results of the depth profiles shown in Figure 6. First, using the assumptions described above with respect to the depth profiles of SEI formed from EC/DEC electrolyte shown in Figure 3, we observe that the concentration of both H^- and $m/z \sim 2$ u negative secondary ions was consistent over the entire SEI. We assume the $m/z \sim 2$ is a convolution of signal from H_2^- and D^- mass fragments for the dPC experiments because Figure 5 clearly shows that deuterated SEI species were present in these depth profiles. The increase in signal for all three depth profiles near the surface of the SEI results from matrix effects common in organic films, and the small increase in signal near the SEI/silicon interface is the result of back reflection effects. In the case of the SEI formed from dPC electrolytes, D^- fragments were distributed throughout, from the surface of the SEI, to the interface of the SEI with the silicon electrode.

The other interpretation of the results shown in Figure 6 is that the signals, or at the least the steady-state signals[59] (e.g., the signal from 20 to 80 depth %), represent the relative concentrations of H^- ions compared to the sum of H_2^- and D^- ions. Work by Minami et al.[90] on organic polymer films used these methods to determine the relative concentration of deuterium-containing and non-deuterium-containing polymer species in ordered (layered) and disordered polymer films. In this interpretation, Figure 6a shows the relative concentration of H^-. The control experiment shows roughly the same or greater concentration of H^- for the length of the profile as that of the SEI formed by PC first and dPC second. The SEI formed by dPC first and PC second shows the lowest H^- yield of the three. In Figure 6b, the trend is reversed. SEI formed by dPC first and PC second has the highest yield for the majority of the depth profile; SEI formed by PC first and dPC second has the second highest ion concentration, and the control SEI has the lowest H_2^-/D^- ion concentration. If deuterium played no role in the increase in ion yield for the $m/z \sim 2$ mass fragment, then one might predict that the signal for the $m/z \sim 2$ ion would match the same trends as those of H^- (as it seems reasonable to assume that H_2^- concentration must be correlated with H^-). The fact that we do not observe this trend supports the hypothesis that the ion signal is proportional to the concentration and that deuterated SEI species are concentrated roughly evenly along the whole length of the SEI. Therefore, the deuterated solvent must be able to be transported through the entirety of the SEI, from the electrolyte to the electrode surface, through both organic and inorganic strata.

3.6. SEI Structure on Silicon Surfaces and Li_2O Formation. We have shown that the SEI structure and composition depends on both the silicon surface chemistry and the state of lithiation of the electrode on which it is formed. From the electrochemical characterization of the etched and native-oxide silicon electrode systems, it is clear that they both share similar lithiation behavior (in terms of lithiation potentials), but their surface reactions are certainly different (as per the electrochemistry shown in Figure 1). Etched silicon electrode surfaces that lack oxide have thicker SEI and an increase in inorganic species, primarily Li_2O and related functionalities.

From our results and work by others,[26,70−73,91−95] there is a preponderance of evidence that the SEI evolves on the surface of silicon electrodes; we emphasize that the results presented here show that electrode surface chemistry plays an integral role in this process. Although the SEI initially forms in the first cycle during lithiation, lithium continues to be consumed throughout cycling, leading to capacity fade.[12] Much work has been done linking the dynamic nature of silicon active material (cracking, swelling) to the stability of the SEI.[22,96] We do not dispute that mechanical factors are of great importance in considering the loss of electrical contact between current collector and active material in composite electrodes. However, we propose that neglecting surface chemistry leads to an incomplete understanding of capacity fade, which occurs on the order of small percentages that compound over the cycle life of the electrode.[12] Often, when surface chemistry is considered, such as in the use of coatings, the explanation of their effectiveness is in a coating's compressive function to suppress SEI cracking with cycling and thus continued reduction and SEI growth in each additional cycle.[97] We have observed that thick, Li_2O-abundant SEI form after a single potential step (lithiation) on the etched electrodes, but under the same conditions, native-oxide silicon electrodes do not produce this SEI composition and structure. While it may be possible to argue that mechanical forces play a role in the breakup of the surface of the etched silicon electrode and produce a thicker SEI, this is

very different from the mechanisms suggested in the literature, which rely on degradation due to repeated cycling. Furthermore, it is likely that mechanical processes are of minimal importance in the results we have presented, as both electrodes experience similar mechanical effects, as seen by the suppressed initial lithiation during cyclic voltammetry (Figure 1).

The question of how and why the Li_2O forms is tied to the surface chemistry and state of lithiation of the electrode. Because Li_2O is found in most abundance on the lithiated etched silicon electrode, it cannot be a product of lithium reacting with silicon oxide (Figures 2 and 3). Furthermore, because Li_2O was much less abundant on the etched, delithiated electrodes, its formation must be reversible to a degree. The source of the lithium must be from solution or SEI species, and we suggest that the source of the oxygen is from the carbonate solvent or organic SEI products. The only other possible source of oxygen is from trace amounts of oxygen in the glovebox during lithiation, but this seems highly unlikely, as this would be very entropically unfavorable, given the concentration of oxygen (5 ppm or less).

If the source of the Li_2O (and/or related lithium hydroxide and peroxide species) is from the solvent, then the mechanism of how it forms is not obvious. We have shown that the SEI is heterogeneous, and porous. The porous nature of the SEI has also been investigated by Harris, Lu, and co-workers[31−33] and Sheldon and co-works.,[34,35] among others. In order for the SEI to grow to the thicknesses we observe, solvent must be transported through the SEI and then decompose at the interface between the SEI and the electrode; therefore, not only the organic but also the inorganic layers must be porous to some degree. From all of these observations, we conclude that the SEI evolves by (1) solvent cointercalating with Li into the SEI, followed by electroreduction, and (2) continued transformation of the SEI products themselves, resulting in the layered strata of SEI functionalities. Electrolyte, or previously insoluble oligomeric/polymeric species, is either electroreduced or thermally decomposed to form soluble products like CO, CO_2, ethylene, methylene, and so on, as well as insoluble Li_2O.

The formation of Li_2O is undesirable for a number of reasons. Even if the Li_2O is reversible in the sense that Li^+ is not permanently consumed, the continued breakdown of the solvent and formation of gases with cycling are detrimental to the operation of a sealed cell in a device. Li_2O formation in a galvanostatic cycling experiment would result in overestimation of the capacity of active materials, particularly high-surface-area nanoarchitectures and under fast charging/discharging rates.

It is difficult to isolate whether Li_2O formation results from the increased conductivity of the etched silicon electrode or if Li_2O is suppressed from being formed by the native-oxide or lithiated native-oxide silicon. For example, the lithiated native-oxide may be a compact, stable intermediate stratum (an artificial SEI layer) that enables the formation and kinetic stability of LiF, $P_xO_yF_z$, and organic SEI components without Li_2O. Another explanation is that the high current density of the etched silicon electrode makes available a high concentration of electrons, and the slow kinetics of the desolvation of the lithium and/or lithiation of the silicon allows for continued side reactions to take place and thus Li_2O formation. Here, the oxide chemistry at silicon is important in its role as an insulator, gating the current and thus favoring the formation of the other inorganics and organic species. It is possible that both of these mechanisms play a role in Li_2O formation and that mechanical mechanisms are also coupled to these reactions.

We have begun work to study how the rate of lithiation influences the SEI composition by in situ spectroelectrochemical methods as well as by the methods described in the present article. We have also begun work investigating how surface treatments and electrolyte additives affect the SEI. It is our hope that this work will further explain SEI structure and formation and tie these properties more directly to performance.

4. CONCLUSIONS

By using model systems of etched and native-oxide covered silicon electrodes, we have explored the effects of the native oxide on SEI composition and structure, using anoxic and anhydrous analytical methods. Cyclic voltammetry and XPS showed a difference between etched and native-oxide silicon electrodes in their surface reactions and SEI components. TOF-SIMS depth profiling on flat model systems enabled the quantification of SEI thickness and structure, showing that SEI was thicker on lithiated electrodes and on etched silicon electrodes and that the increase in SEI thickness in the etched samples was due to LiO_x components (which we attributed to Li_2O).

Multivariate analysis (PCA) was used to compare entire mass spectra against each other and highlight the chemical similarities of the outermost layers of all of the SEI as well as the differences in the other strata. Combining the PCA analysis with traditional univariate depth profile analysis, isotope labeling of solvent that participated in SEI formation, and XPS data showed that the SEI is porous, and continued to evolve by solvent transport through the SEI. On etched silicon electrodes, this solvent transport provides a possible source of oxygen for the thick Li_2O stratum found near the SEI/electrode interface. Further work is needed to understand the exact mechanism by which the native oxide prevents this Li_2O stratum from forming. The style of analysis presented here shows promise to help understand the effects of surface coatings and electrolyte additives on SEI structure and composition.

■ ASSOCIATED CONTENT

Supporting Information

XPS spectra with fits, optical profilometry data, and a table of information ranking secondary ion mass fragments by their PCA loadings. This material is available free of charge via the Internet at http://pubs.acs.org.

■ AUTHOR INFORMATION

Corresponding Author

*E-mail: stevenson@cm.utexas.edu.

Notes

The authors declare no competing financial interest.

■ ACKNOWLEDGMENTS

This material is based upon work supported as part of the program "Understanding Charge Separation and Transfer at Interfaces in Energy Materials (EFRC:CST)", an Energy Frontier Research Center funded by the U.S. Department of Energy, Office of Science, Office of Basic Energy Sciences under award no. DE-SC0001091. L.J.W. holds a Career Award at the Scientific Interface from the Burroughs Wellcome Fund

and is an Alfred P. Sloan Research Fellow. K.W.S. thanks Dr. Andrei Dolocan, Dr. Hugo Celio, Judith Alvasados, Dr. Tom Yersak, and Prof. Shirley Meng for their thoughtful discussions concerning these experiments and their results.

REFERENCES

(1) Aurbach, D.; Daroux, M.; Faguy, P.; Yeager, E. The Electrochemistry of Noble Metal Electrodes in Aprotic Organic Solvents Containing Lithium Salts. *J. Electroanal. Chem.* **1991**, *297*, 225−244.
(2) Aurbach, D.; Zaban, A.; Schechter, A.; Ein-Eli, Y.; Zinigrad, E.; Markovsky, B. The Study of Electrolyte Solutions Based on Ethylene and Diethyl Carbonates for Rechargeable Li Batteries. *J. Electrochem. Soc.* **1995**, *142*, 2873−2882.
(3) Aurbach, D.; Daroux, M. L.; Faguy, P. W.; Yeager, E. Identification of Surface Films Formed on Lithium in Dimethoxyethane and Tetrahydrofuran Solutions. *J. Electrochem. Soc.* **1988**, *135*, 1863−1871.
(4) Aurbach, D. Identification of Surface Films Formed on Lithium in Propylene Carbonate Solutions. *J. Electrochem. Soc.* **1987**, *134*, 1611−1620.
(5) Aurbach, D. The Behavior of Lithium Electrodes in Mixtures of Alkyl Carbonates and Ethers. *J. Electrochem. Soc.* **1991**, *138*, 3529−3536.
(6) Aurbach, D.; Ein-Ely, Y.; Zaban, A. The Surface Chemistry of Lithium Electrodes in Alkyl Carbonate Solutions. *J. Electrochem. Soc.* **1994**, *141*, L1−L3.
(7) Peled, E.; Bar Tow, D.; Merson, A.; Burstein, L. Microphase Structure of SEI on HOPG. *J. New Mater.* **2000**, *328*, 321−328.
(8) Peled, E.; Bar Tow, D.; Merson, A.; Gladkich, A.; Burstein, L.; Golodnitsky, D. Composition, Depth Profiles and Lateral Distribution of Materials in the SEI Built on HOPG-TOF SIMS and XPS Studies. *J. Power Sources* **2001**, *97−98*, 52−57.
(9) Peled, E.; Ardel, G.; Golodnitsky, D. Advanced Model for Solid Electrolyte Interphase Electrodes in Liquid and Polymer Electrolytes. *J. Electrochem. Soc.* **1997**, *144*, L208−L210.
(10) Verma, P.; Maire, P.; Novák, P. A Review of the Features and Analyses of the Solid Electrolyte Interphase in Li-Ion Batteries. *Electrochim. Acta* **2010**, *55*, 6332−6341.
(11) Kim, S.; van Duin, A. C. T.; Shenoy, V. B. Effect of Electrolytes on the Structure and Evolution of the Solid Electrolyte Interphase (SEI) in Li-Ion Batteries: A Molecular Dynamics Study. *J. Power Sources* **2011**, *196*, 8590−8597.
(12) Deshpande, R.; Verbrugge, M. W.; Cheng, Y.-T.; Wang, J.; Liu, P. Battery Cycle Life Prediction with Coupled Chemical Degradation and Fatigue Mechanics. *J. Electrochem. Soc.* **2012**, *159*, A1730−A1738.
(13) Gachot, G.; Grugeon, S.; Eshetu, G. G.; Mathiron, D.; Ribière, P.; Armand, M.; Laruelle, S. Thermal Behaviour of the Lithiated-Graphite/Electrolyte Interface through GC/MS Analysis. *Electrochim. Acta* **2012**, *83*, 402−409.
(14) Nie, M.; Abraham, D. P.; Chen, Y.; Bose, A.; Lucht, B. L. Silicon Solid Electrolyte Interphase (SEI) of Lithium Ion Battery Characterized by Microscopy and Spectroscopy. *J. Phys. Chem. C* **2013**, *117*, 13403−13412.
(15) Schroder, K. W.; Celio, H.; Webb, L. J.; Stevenson, K. J. Examining Solid Electrolyte Interphase Formation on Crystalline Silicon Electrodes: Influence of Electrochemical Preparation and Ambient Exposure Conditions. *J. Phys. Chem. C* **2012**, *116*, 19737−19747.
(16) Malmgren, S.; Ciosek, K.; Lindblad, R.; Plogmaker, S.; Kühn, J.; Rensmo, H.; Edström, K.; Hahlin, M. Consequences of Air Exposure on the Lithiated Graphite SEI. *Electrochim. Acta* **2013**, *105*, 83−91.
(17) Cresce, A. v.; Russell, S. M.; Baker, D. R.; Gaskell, K. J.; Xu, K. In Situ and Quantitative Characterization of Solid Electrolyte Interphases. *Nano Lett.* **2014**, *14*, 1405−1412.
(18) Veryovkin, I. V.; Tripa, C. E.; Zinovev, A. V.; Baryshev, S. V.; Li, Y.; Abraham, D. P. TOF SIMS Characterization of SEI Layer on Battery Electrodes. *Nucl. Instrum. Methods Phys. Res., Sect. B* **2014**, *332*, 368−372.
(19) Philippe, B.; Dedryvère, R.; Allouche, J.; Lindgren, F.; Gorgoi, M.; Rensmo, H.; Gonbeau, D.; Edström, K. Nanosilicon Electrodes for Lithium-Ion Batteries: Interfacial Mechanisms Studied by Hard and Soft X-ray Photoelectron Spectroscopy. *Chem. Mater.* **2012**, *24*, 1107−1115.
(20) Key, B.; Bhattacharyya, R.; Morcrette, M.; Seznéc, V.; Tarascon, J.-M.; Grey, C. P. Real-Time NMR Investigations of Structural Changes in Silicon Electrodes for Lithium-Ion Batteries. *J. Am. Chem. Soc.* **2009**, *131*, 9239−9249.
(21) Kim, T.; Park, S.; Oh, S. M. Solid-State NMR and Electrochemical Dilatometry Study on Li^+ Uptake/Extraction Mechanism in SiO Electrode. *J. Electrochem. Soc.* **2007**, *154*, A1112−A1117.
(22) Wu, H.; Chan, G.; Choi, J. W.; Ryu, I.; Yao, Y.; McDowell, M. T.; Lee, S. W.; Jackson, A.; Yang, Y.; Hu, L.; Cui, Y. Stable Cycling of Double-Walled Silicon Nanotube Battery Anodes through Solid-Electrolyte Interphase Control. *Nat. Nanotechnol.* **2012**, *7*, 310−315.
(23) Xun, S.; Song, X.; Wang, L.; Grass, M. E.; Liu, Z.; Battaglia, V. S.; Liu, G. The Effects of Native Oxide Surface Layer on the Electrochemical Performance of Si Nanoparticle-Based Electrodes. *J. Electrochem. Soc.* **2011**, *158*, A1260−A1266.
(24) Lucas, I. T.; Syzdek, J.; Kostecki, R. Interfacial Processes at Single-Crystal β-Sn Electrodes in Organic Carbonate Electrolytes. *Electrochem. Commun.* **2011**, *13*, 1271−1275.
(25) Qiao, R.; Lucas, I. T.; Karim, A.; Syzdek, J.; Liu, X.; Chen, W.; Persson, K.; Kostecki, R.; Yang, W. Distinct Solid-Electrolyte-Interphases on Sn (100) and (001) Electrodes Studied by Soft X-Ray Spectroscopy. *Adv. Mater. Interfaces* **2014**, *1*, 1300115.
(26) Lucas, I. T.; Pollak, E.; Kostecki, R. In Situ AFM Studies of SEI Formation at a Sn Electrode. *Electrochem. Commun.* **2009**, *11*, 2157−2160.
(27) Xiao, X.; Lu, P.; Ahn, D. Ultrathin Multifunctional Oxide Coatings for Lithium Ion Batteries. *Adv. Mater.* **2011**, *23*, 1−5.
(28) Graham, D. J.; Castner, D. G. Multivariate Analysis of ToF-SIMS Data from Multicomponent Systems: The Why, When, and How. *Biointerphases* **2012**, *7*, 49−61.
(29) Pacholski, M. L. Principal Component Analysis of TOF-SIMS Spectra, Images and Depth Profiles: An Industrial Perspective. *Appl. Surf. Sci.* **2004**, *231−232*, 235−239.
(30) Muramoto, S.; Graham, D. J.; Wagner, M. S.; Lee, T. G.; Moon, D. W.; Castner, D. G. ToF-SIMS Analysis of Adsorbed Proteins: Principal Component Analysis of the Primary Ion Species Effect on the Protein Fragmentation Patterns. *J. Phys. Chem. C* **2011**, *115*, 24247−24255.
(31) Lu, P.; Harris, S. J. Lithium Transport within the Solid Electrolyte Interphase. *Electrochem. Commun.* **2011**, *13*, 1035−1037.
(32) Lu, P.; Li, C.; Schneider, E. W.; Harris, S. J. Chemistry, Impedance, and Morphology Evolution in Solid Electrolyte Interphase Films during Formation in Lithium Ion Batteries. *J. Phys. Chem. C* **2014**, *118*, 896−903.
(33) Shi, S.; Lu, P.; Liu, Z.; Qi, Y.; Hector, L. G.; Li, H.; Harris, S. J. Direct Calculation of Li-Ion Transport in the Solid Electrolyte Interphase. *J. Am. Chem. Soc.* **2012**, *134*, 15476−15487.
(34) Tokranov, A.; Sheldon, B. W.; Li, C.; Minne, S.; Xiao, X. In Situ Atomic Force Microscopy Study of Initial Solid Electrolyte Interphase Formation on Silicon Electrodes for Li-Ion Batteries. *ACS Appl. Mater. Interfaces* **2014**, *6*, 6672−6686.
(35) Soni, S. K.; Sheldon, B. W.; Xiao, X.; Bower, A. F.; Verbrugge, M. W. Diffusion Mediated Lithiation Stresses in Si Thin Film Electrodes. *J. Electrochem. Soc.* **2012**, *159*, A1520−A1527.
(36) Celio, H.; et al. Interface Designed with Differential Pumping and Built-in Figure of Merit Method to Monitor Chambers where Environmentally Sensitive Samples are Prepared and Transferred for Analysis. U.S. Patent 14/445,650, 2014.
(37) Beamson, G.; Briggs, D. *High Resolution XPS of Organic Polymers: The Scienta ESCA300 Database*; John Wiley & Sons: New York, 1992; Vol. *15*.

(38) Leung, T. Y.; Man, W. F.; Lim, P. K.; Chan, W. C.; Gaspari, F.; Zukotynski, S. Determination of the sp^3/sp^2 Ratio of a-C:H by XPS and XAES. *J. Non-Cryst. Solids* **1999**, *254*, 156−160.
(39) Edström, K.; Gustafsson, T.; Thomas, J. O. The Cathode−Electrolyte Interface in the Li-Ion Battery. *Electrochim. Acta* **2004**, *50*, 397−403.
(40) Philippe, B.; Dedryvère, R.; Gorgoi, M.; Rensmo, H.; Gonbeau, D.; Edström, K.; Dedryvere, R.; Edstrom, K. Improved Performances of Nanosilicon Electrodes Using the Salt LiFSI: A Photoelectron Spectroscopy Study. *J. Am. Chem. Soc.* **2013**, *135*, 9829−9842.
(41) Green, F. M.; Gilmore, I. S.; Seah, M. P. TOF-SIMS: Accurate Mass Scale Calibration. *J. Am. Soc. Mass Spectrom.* **2006**, *17*, 514−523.
(42) Perez, F.; Granger, B. E. IPython: A System for Interactive Scientific Computing. *Comput. Sci. Eng.* **2007**, *9*, 21−29.
(43) Van der Walt, S.; Colbert, S. C.; Varoquaux, G. The NumPy Array: A Structure for Efficient Numerical Computation. *Comput. Sci. Eng.* **2011**, *13*, 22−30.
(44) Jones, E.; Oliphant, T.; Peterson, P.; et al. *SciPy: Open Source Scientific Tools for Python*; http://www.scipy.org/.
(45) McKinney, W. Data Structures for Statistical Computing in Python, SciPy 2010 Pyton for Scientific Computing Conference, Austin, Texas, June 28−July 3, 2010; pp 51−56.
(46) Zimmerman, J. D.; Lassiter, B. E.; Xiao, X.; Sun, K.; Dolocan, A.; Gearba, R.; Vanden Bout, D. A.; Stevenson, K. J.; Wickramasinghe, P.; Thompson, M. E.; Forrest, S. R. Control of Interface Order by Inverse Quasi-Epitaxial Growth of Squaraine/fullerene Thin Film Photovoltaics. *ACS Nano* **2013**, *7*, 9268−9275.
(47) Elko-Hansen, T. D.-M.; Dolocan, A.; Ekerdt, J. G. Atomic Interdiffusion and Diffusive Stabilization of Cobalt by Copper during Atomic Layer Deposition from Bis(*N*-*tert*-butyl-*N*′-ethylpropionamidinato) Cobalt(II). *J. Phys. Chem. Lett.* **2014**, *5*, 1−9.
(48) Radvanyi, E.; De Vito, E.; Porcher, W.; Danet, J.; Desbois, P.; Colin, J.-F.; Si Larbi, S. J. Study of Lithiation Mechanisms in Silicon Electrodes by Auger Electron Spectroscopy. *J. Mater. Chem. A* **2013**, *1*, 4956−4965.
(49) Radvanyi, E.; Porcher, W.; De Vito, E.; Montani, A.; Franger, S.; Si Larbi, S. J. Failure Mechanisms of Nano-Silicon Anodes upon Cycling: An Electrode Porosity Evolution Model. *Phys. Chem. Chem. Phys.* **2014**, *16*, 17142−17153.
(50) Radvanyi, E.; De Vito, E.; Porcher, W.; Si Larbi, S. J. An XPS/AES Comparative Study of the Surface Behaviour of Nano-Silicon Anodes for Li-Ion Batteries. *J. Anal. At. Spectrom.* **2014**, *29*, 1120−1131.
(51) McDowell, M. T.; Lee, S. W.; Harris, J. T.; Korgel, B. A.; Wang, C.; Nix, W. D.; Cui, Y. In-Situ TEM of Two-Phase Lithiation of Amorphous Silicon Nanospheres. *Nano Lett.* **2013**, *13*, 758−764.
(52) Limthongkul, P.; Jang, Y.-I.; Dudney, N. J.; Chiang, Y.-M. Electrochemically-Driven Solid-State Amorphization in Lithium-Silicon Alloys and Implications for Lithium Storage. *Acta Mater.* **2003**, *51*, 1103−1113.
(53) Limthongkul, P.; Jang, Y.-I.; Dudney, N. J.; Chiang, Y.-M. Electrochemically-Driven Solid-State Amorphization in Lithium−Metal Anodes. *J. Power Sources* **2003**, *119*−*121*, 604−609.
(54) Gu, M.; Wang, Z.; Connell, J. G.; Perea, D. E.; Lauhon, L. J.; Gao, F.; Wang, C. Electronic Origin for the Phase Transition from Amorphous Li_xSi to Crystalline $Li_{15}Si_4$. *ACS Nano* **2013**, *7*, 6303−6309.
(55) Chan, M. K. Y.; Wolverton, C.; Greeley, J. P. First Principles Simulations of the Electrochemical Lithiation and Delithiation of Faceted Crystalline Silicon. *J. Am. Chem. Soc.* **2012**, *134*, 14362−14374.
(56) Corso, B. L.; Perez, I.; Sheps, T.; Sims, P. C.; Gül, O. T.; Collins, P. G. Electrochemical Charge-Transfer Resistance in Carbon Nanotube Composites. *Nano Lett.* **2014**, *14*, 1329−1336.
(57) Cheng, Y.-T.; Verbrugge, M. W. Diffusion-Induced Stress, Interfacial Charge Transfer, and Criteria for Avoiding Crack Initiation of Electrode Particles. *J. Electrochem. Soc.* **2010**, *157*, A508−A516.
(58) Bazant, M. Z. Theory of Chemical Kinetics and Charge Transfer Based on Nonequilibrium Thermodynamics. *Acc. Chem. Res.* **2013**, *46*, 1144−1160.
(59) Cheng, J.; Wucher, A.; Winograd, N. Molecular Depth Profiling with Cluster Ion Beams. *J. Phys. Chem. B* **2006**, *110*, 8329−8336.
(60) Cheng, J.; Winograd, N. Depth Profiling of Peptide Films with TOF-SIMS and a C_{60} Probe. *Anal. Chem.* **2005**, *77*, 3651−3659.
(61) Brison, J.; Muramoto, S.; Castner, D. G. ToF-SIMS Depth Profiling of Organic Films: A Comparison between Single Beam and Dual-Beam Analysis. *J. Phys. Chem. C* **2010**, *114*, 5565−5573.
(62) Cramer, H.-G.; Grehl, T.; Kollmer, F.; Moellers, R.; Niehuis, E.; Rading, D. Depth Profiling of Organic Materials Using Improved Ion Beam Conditions. *Appl. Surf. Sci.* **2008**, *255*, 966−969.
(63) Seah, M. P.; Green, F. M.; Gilmore, I. S. Cluster Primary Ion Sputtering: Secondary Ion Intensities in Static SIMS of Organic Materials. *J. Phys. Chem. C* **2010**, *114*, 5351−5359.
(64) Gillen, G.; Roberson, S. Preliminary Evaluation of an SF_5^+ Polyatomic Primary Ion Beam for Analysis of Organic Thin Films by Secondary Ion Mass Spectrometry. *Rapid Commun. Mass Spectrom.* **1998**, *12*, 1303−1312.
(65) Bulle-Lieuwma, C.; van Gennip, W. J. H.; van Duren, J. K. J.; Jonkheijm, P.; Janssen, R. A. J.; Niemantsverdriet, J. W. Characterization of Polymer Solar Cells by TOF-SIMS Depth Profiling. *Appl. Surf. Sci.* **2003**, *203*−*204*, 547−550.
(66) Ninomiya, S.; Ichiki, K.; Yamada, H.; Nakata, Y.; Seki, T.; Aoki, T.; Matsuo, J. Precise and Fast Secondary Ion Mass Spectrometry Depth Profiling of Polymer Materials with Large Ar Cluster Ion Beams. *Rapid Commun. Mass Spectrom.* **2009**, *23*, 1601−1606.
(67) Piwowar, A. M.; Lockyer, N. P.; Vickerman, J. C. Salt Effects on Ion Formation in Desorption Mass Spectrometry: An Investigation into the Role of Alkali Chlorides on Peak Suppression in Time-of-Flight-Secondary Ion Mass Spectrometry. *Anal. Chem.* **2009**, *81*, 1040−1048.
(68) Gnaser, H. Ionization Probability of Sputtered Negative Cluster Ions: Dependence on Surface Work Function and Emission Velocity. *Phys. Rev. B* **2001**, *63*, 045415−1−045415−045417.
(69) Aurbach, D.; Markovsky, B.; Weissman, I.; Levi, E.; Ein-Eli, Y. On the Correlation between Surface Chemistry and Performance of Graphite Negative Electrodes for Li Ion Batteries. *Electrochim. Acta* **1999**, *45*, 67−86.
(70) Martínez de la Hoz, J. M.; Balbuena, P. B. Reduction Mechanisms of Additives on Si Anodes of Li-Ion Batteries. *Phys. Chem. Chem. Phys.* **2014**, *16*, 17091−17098.
(71) Ma, Y.; Balbuena, P. B. DFT Study of Reduction Mechanisms of Ethylene Carbonate and Fluoroethylene Carbonate on Li^+-Adsorbed Si Clusters. *J. Electrochem. Soc.* **2014**, *161*, E3097−E3109.
(72) Martínez de la Hoz, J. M.; Leung, K.; Balbuena, P. B. Reduction Mechanisms of Ethylene Carbonate on Si Anodes of Lithium-Ion Batteries: Effects of Degree of Lithiation and Nature of Exposed Surface. *ACS Appl. Mater. Interfaces* **2013**, *5*, 13457−13465.
(73) Leung, K.; Rempe, S. B.; Foster, M. E.; Ma, Y.; Martínez del la Hoz, J. M.; Sai, N.; Balbuena, P. B. Modeling Electrochemical Decomposition of Fluoroethylene Carbonate on Silicon Anode Surfaces in Lithium Ion Batteries. *J. Electrochem. Soc.* **2013**, *161*, A213−A221.
(74) Besenhard, J. O.; Winter, M.; Yang, J.; Biberacher, W. Filming Mechanism of Lithium-Carbon Anodes in Organic and Inorganic Electrolytes. *J. Power Sources* **1995**, *54*, 228−231.
(75) Wrodnigg, G. H.; Wrodnigg, T. M.; Besenhard, J. O.; Winter, M. Propylene Sulfite as Film-Forming Electrolyte Additive in Lithium Ion Batteries. *Electrochem. Commun.* **1999**, *1*, 148−150.
(76) Peled, E.; Golodnitsky, D. In *Lithium-Ion Batteries: Solid-Electrolyte Interphase*; Balbuena, P. B., Wang, Y., Eds.; Imperial College Press: London, 2004.
(77) Wang, Q.; Sun, J.; Yao, X.; Chen, C. Thermal Stability of $LiPF_6$/EC+DEC Electrolyte with Charged Electrodes for Lithium Ion Batteries. *Thermochim. Acta* **2005**, *437*, 12−16.

(78) Yang, H.; Zhuang, G. V.; Ross, P. N. Thermal Stability of $LiPF_6$ Salt and Li-Ion Battery Electrolytes Containing $LiPF_6$. *J. Power Sources* **2006**, *161*, 573−579.
(79) Zinigrad, E.; Larush-Asraf, L.; Gnanaraj, J. S.; Sprecher, M.; Aurbach, D. On the Thermal Stability of $LiPF_6$. *Thermochim. Acta* **2005**, *438*, 184−191.
(80) Henderson, A.; Fletcher, J. S.; Vickerman, J. C. A Comparison of PCA and MAF for ToF-SIMS Image Interpretation. *Surf. Interface Anal.* **2009**, *41*, 666−674.
(81) Keenan, M. R.; Kotula, P. G. Accounting for Poisson Noise in the Multivariate Analysis of ToF-SIMS Spectrum Images. *Surf. Interface Anal.* **2004**, *36*, 203−212.
(82) Miyasaka, T.; Ikemoto, T.; Kohno, T. ToF-SIMS Imaging of PE/PP Polymer Using Multivariate Analysis. *Appl. Surf. Sci.* **2008**, *255*, 1576−1579.
(83) Redman, D. W.; Murugesan, S.; Stevenson, K. J. Cathodic Electrodeposition of Amorphous Elemental Selenium from an Air- and Water-Stable Ionic Liquid. *Langmuir* **2014**, *30*, 418−425.
(84) Rahner, D.; Machill, S.; Ludwig, G. Characterization of Lithium and Electrolytes by Electrochemical Impedance Spectroscopy. *J. Power Sources* **1995**, *54*, 378−382.
(85) Aurbach, D. In *Advances in Lithium-Ion Batteries*; Schalkwijk, W. A.,Scrosati, B., Eds.; Kluwer Academic Publishers: Boston, MA, 2002.
(86) Peled, E. In *Lithium Batteries*; Gabano, J.-P., Ed.; Academic Press: New York, 1983.
(87) MacNeil, D. D. Comparison of the Reactivity of Various Carbon Electrode Materials with Electrolyte at Elevated Temperature. *J. Electrochem. Soc.* **1999**, *146*, 3596.
(88) Dahn, J. R.; Fong, R.; Spoon, M. Suppression of Staging in Lithium-Intercalated Carbon by Disorder in The Host. *Phys. Rev. B* **1990**, *42*, 6424−6432.
(89) Favors, Z.; Wang, W.; Bay, H. H.; George, A.; Ozkan, M.; Ozkan, C. S. Stable Cycling of SiO_2 Nanotubes as High-Performance Anodes for Lithium-Ion Batteries. *Sci. Rep.* **2014**, *4*, 4605.
(90) Minami, I.; Kubo, T.; Fujiwara, S.; Ogasawara, Y.; Nanao, H.; Mori, S. Investigation of Tribo-Chemistry by Means of Stable Isotopic Tracers: TOF-SIMS Analysis of Langmuir−Blodgett Films and Examination of Their Tribological Properties. *Tribol. Lett.* **2005**, *20*, 287−297.
(91) Bryngelsson, H.; Stjerndahl, M.; Gustafsson, T.; Edström, K. How Dynamic Is the SEI? *J. Power Sources* **2007**, *174*, 970−975.
(92) Tavassol, H.; Buthker, J. W.; Ferguson, G. A.; Curtiss, L. A.; Gewirth, A. A. Solvent Oligomerization during SEI Formation on Model Systems for Li-Ion Battery Anodes. *J. Electrochem. Soc.* **2012**, *159*, A730−A738.
(93) Leifer, N.; Smart, M. C.; Prakash, G. K. S.; Gonzalez, L.; Sanchez, L.; Smith, K. A.; Bhalla, P.; Grey, C. P.; Greenbaum, S. G. ^{13}C Solid State NMR Suggests Unusual Breakdown Products in SEI Formation on Lithium Ion Electrodes. *J. Electrochem. Soc.* **2011**, *158*, A471−A480.
(94) Herstedt, M.; Abraham, D. P.; Kerr, J. B.; Edström, K. X-ray Photoelectron Spectroscopy of Negative Electrodes from High-Power Lithium-Ion Cells Showing Various Levels of Power Fade. *Electrochim. Acta* **2004**, *49*, 5097−5110.
(95) Benitez, L.; Cristancho, D.; Seminario, J. M.; Martínez de la Hoz, J. M.; Balbuena, P. B. Electron Transfer through Solid-Electrolyte-Interphase Layers Formed on Si Anodes of Li-Ion Batteries. *Electrochim. Acta* **2014**, *140*, 250−257.
(96) Zheng, G.; Lee, S. W.; Liang, Z.; Lee, H.-W.; Yan, K.; Yao, H.; Wang, H.; Li, W.; Chu, S.; Cui, Y. Interconnected Hollow Carbon Nanospheres for Stable Lithium Metal Anodes. *Nat. Nanotechnol.* **2014**, 1−6.
(97) Mukhopadhyay, A.; Sheldon, B. W. Deformation and Stress in Electrode Materials for Li-Ion Batteries. *Prog. Mater. Sci.* **2014**, *63*, 58−116.